JOURNAL OF MATERIALS SCIENCE 32 (1997) 3089–3099

Microstructure of vapour quenched Ti–29 wt % Mg alloy solid solution

J. G. ZHENG, P. G. PARTRIDGE, J. W. STEEDS
H.H. Wills Physics Laboratory, University of Bristol, Tyndall Avenue, Bristol BS8 1TL, UK
D. M. J. WILKES, C. M. WARD-CLOSE
Structural Materials Centre, Defence Research Agency, Farnborough, Hants, GU14 6TD, UK

A Ti–29 wt% Mg (Ti–45 at% Mg) alloy produced by vapour quenching has been studied using scanning electron microscopy, transmission electron microscopy, energy dispersive X-ray spectroscopy, imaging parallel electron energy-loss spectroscopy and electron diffraction. The alloy is shown to be composed of highly supersaturated solid solutions between two elements hitherto believed to be immiscible. It has a microstructure consisting of columnar units, columnar grains, columnar subgrains, herring-bone patterns and parallel stripes ranging in size from 15 μm to 2 nm. Superimposed on the microstructure are periodic compositional bands with a period of ~ 0.5 μm. The origins of the periodic compositional bands and the herring-bone patterns are discussed.

1. Introduction

Light-weight structural materials are becoming increasingly important in transportation and aerospace applications [1]. A considerable number of studies on titanium have focused on reducing its density ($\rho = 4.5 \times 10^3$ kg m^{-3}) and increasing its specific strength by alloying with lighter elements. The addition of magnesium ($\rho = 1.47 \times 10^3$ kg m^{-3}) is particularly attractive, but since the boiling point of magnesium (1380 K) is much lower than the melting point of titanium (1941 K), conventional melting techniques are precluded. Magnesium also has a negligible equilibrium solid solubility in titanium and this appears to rule out alloying using techniques such as conventional powder metallurgy, rapid solidification and solid-state processing [2–8]. However, with the exception of valency, the alloying factors such as atomic size, crystal structure and electronegativity favour extensive solid solution in this system [9].

Recently, attention has been focused on the application of mechanical alloying [10–12] and physical vapour deposition [1, 13–16] techniques. Metastable supersaturated Ti–Mg alloy solid solutions with magnesium concentrations up to 24 wt % have been successfully produced using mechanical alloying whilst contents of up to 60 wt % have been achieved by the use of physical vapour deposition. The alloys produced using this latter technique show attractive mechanical properties and a low density. Structural information on these alloys was mainly obtained by X-ray diffraction and transmission electron microscopy (TEM). The X-ray diffraction experiments showed that the diffraction peaks from these alloys shifted towards lower diffraction angles and became fewer and broader with increasing Mg content [13]. At magnesium concentrations between 25–50 wt %, the X-ray data were ambiguous because of the existence of very broad overlapping diffraction peaks. These broad peaks were attributed to a high dislocation density, high residual stress and small grain size [13]. Subsequent TEM studies on the dilute Ti–rich and Mg rich solid solutions showed that annealing or hot–pressing at 500 °C or higher resulted in the precipitation of Mg or Ti from the solid solution [14–16]. More detailed information is needed to clarify the microstructure in these highly supersaturated Ti–Mg alloys, especially in those with a magnesium concentration between 25–50 wt %. An analytical transmission electron microscope equipped with energy dispersive X-ray (EDX) analysis and imaging parallel electron energy loss spectroscopy (PEELS) has proved to be an effective tool for studying light elements at a high spatial resolution. These techniques are used in this paper to characterize the microstructure of a vapour quenched Ti–Mg alloy with an average magnesium content of 29 wt %.

2. Experimental procedure

A Ti–29 wt % Mg alloy was produced by evaporating titanium and magnesium from separate sources and mixing the vapours before condensation onto a heated Ti substrate maintained at 300 °C. Titanium was evaporated from a rod-fed titanium source by an electron beam and the radiantly heated magnesium source was positioned around and above the titanium source, as has been previously described [1]. The as-deposited Ti–Mg alloy was 1.8 mm thick. The deposit growth surface (perpendicular to the growth direction) and fracture surfaces (parallel to this direction) were observed in a Jeol JSM-6400 scanning electron microscope operated at 20 keV. TEM experiments were

0022–2461

carried out on Philips EM430 and Hitachi HF2000 microscopes. The latter was equipped with a cold field emission gun, EDX spectroscopy and imaging PEELS. Thin foils for TEM observations were prepared by cutting the as-deposited sample parallel and normal to the deposit growth directions into slices 0.5 mm thick, mechanically grinding the slices to 40 nm, dimpling them to 15 nm and ion milling them on a cold stage to TEM transparency.

3. Results

3.1. Scanning electron microscopy (SEM)

The columnar microstructure in a fracture surface parallel to the deposit growth direction G (Fig. 1a) shows that the alloy is composed of columnar units with axes nearly parallel to G. The columnar units taper at the deposit growth surface (Figs. 1(a and b)), appear to be 7–15 μm in diameter and have steps on their inclined growth surfaces (Fig. 1c). Within columnar units, whose fractured sections are shown in Fig. 1d, there are columnar grains of about 1–4 μm in diameter. Fig. 2(a and b) schematically illustrates the configuration of columnar units and columnar grains in sections normal and parallel to G. Fig. 2(a and b) also illustrates voids at grain boundaries, columnar subgrains and a herring-bone pattern, all of which will be discussed in the next section.

3.2. Transmission electron microscopy (TEM)

More information about the columnar microstructure was obtained by a TEM investigation of thin foils normal and parallel to the growth direction.

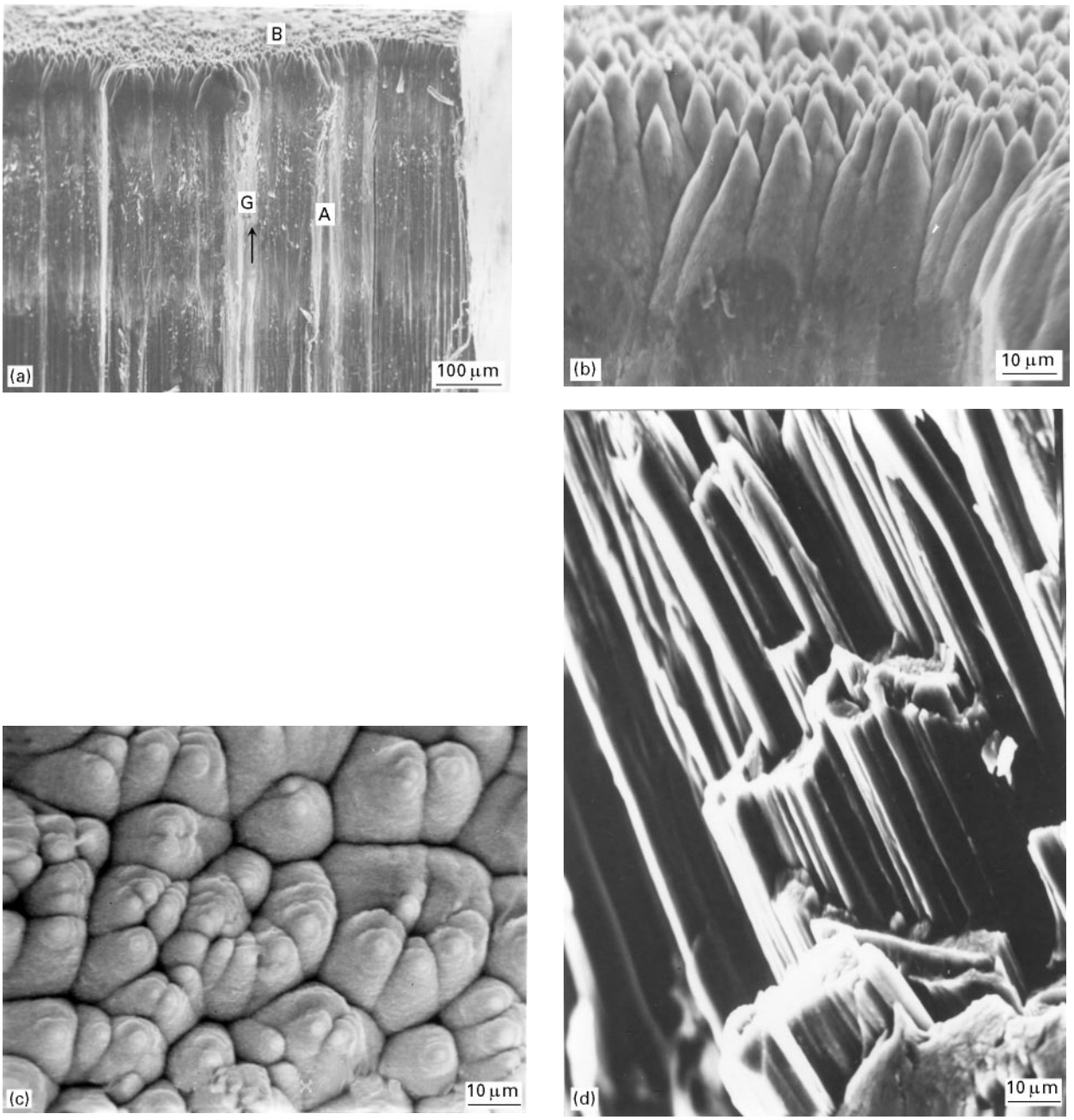

Figure 1 SEM of the columnar microstructure showing (a) fracture surface at A and growth surface at B, parallel and normal to the deposit growth direction G respectively, (b) tapered growth surface of columnar units, (c) top view of the growth surface showing columnar units with surface steps, (d) fractured columnar units containing columnar grains.

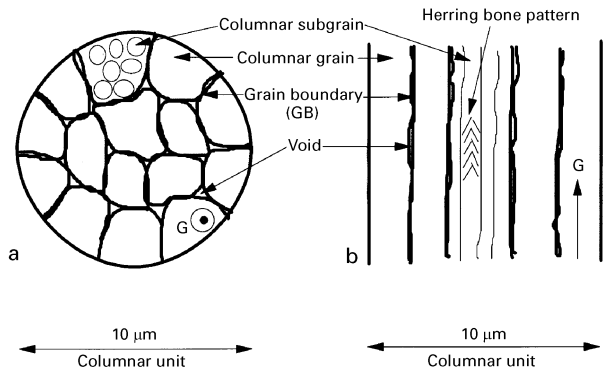

Figure 2 Schematic diagram of columnar unit containing columnar grains, subgrains and herring-bone patterns. Sections (a) normal and (b) parallel to G.

A bright field TEM image of a foil normal to G (Fig. 3a) shows sections through the columnar grains within columnar units and reveals elongated voids at the grain boundaries (see bright contrast at GB). Weak contrast mottling on a scale of about 0.25 μm is visible within the grains, which was caused by a small misorientation between subgrains. Within subgrains there are also brighter and darker contrast regions on a much smaller scale, varying between 5–100 nm (Fig. 3b). This contrast effect will be shown in Section 3.4 to be caused by compositional variations: the brighter regions are Mg–rich and the darker regions Ti-rich.

A bright field TEM image of a foil parallel to G (Fig. 3c) shows columnar grains and grain boundary

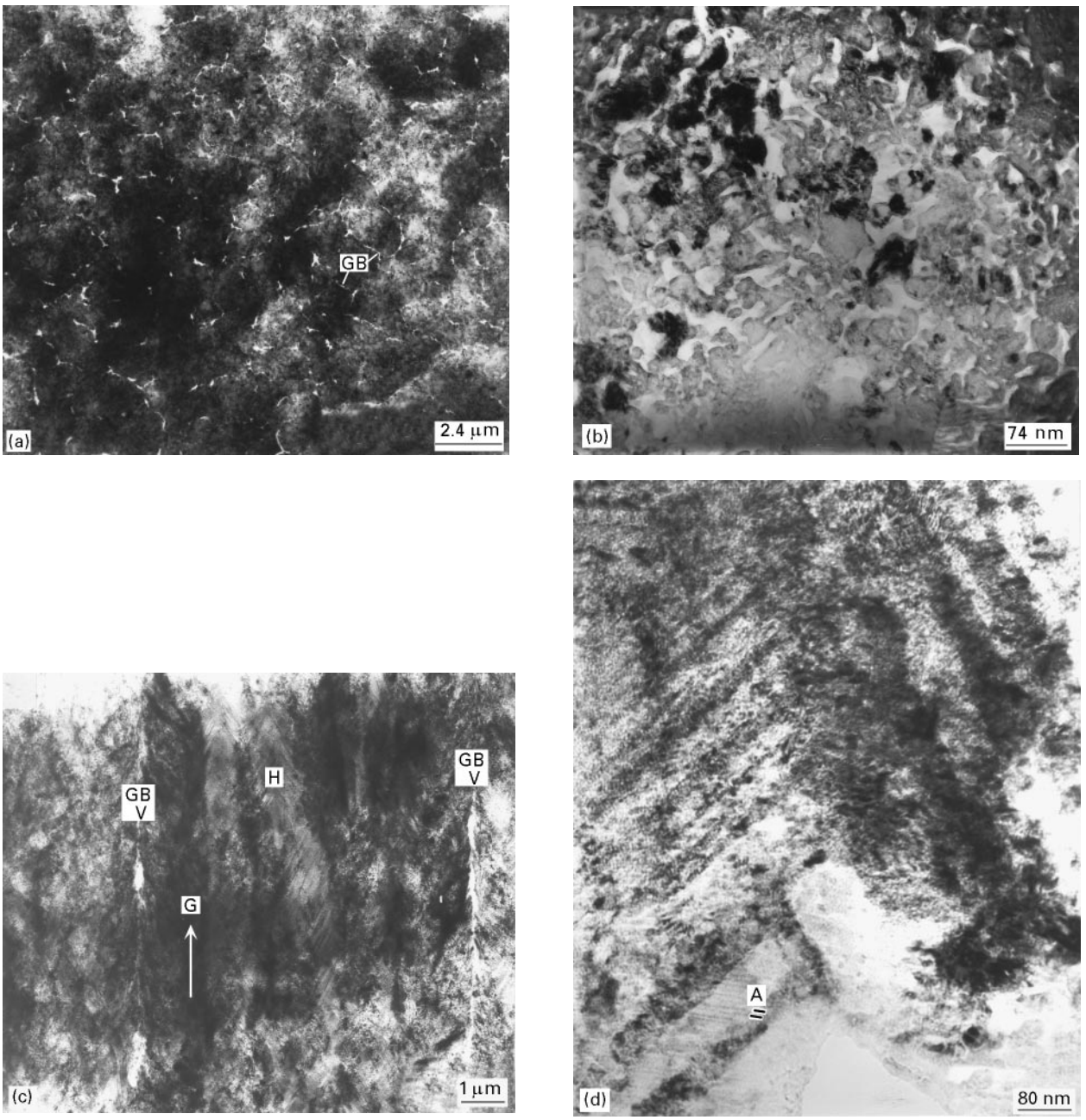

Figure 3 TEM of the columnar microstructure in sections (a) and (b) normal and (c) and (d) parallel to G. (a) Grains, voids at grain boundaries (GB) and subgrain contrast, (b) Compositional contrast within subgrains. (c) columnar grain, GBs, columnar subgrain and herring bone pattern (see at H), (d) enlarged herring bone pattern.

voids (see bright contrast at the columnar grain boundaries GB). The columnar grain contains several columnar subgrains that appear as darker or brighter contrast bands of $\sim 0.25\,\mu m$ width. The incident electron beam was closer to a zone axis in the darker bands than in the brighter ones. Slight tilting of the sample lead to contrast changes of the bands, brighter bands becoming darker and *vice-versa*. This confirms that there was a slight misorientation between the subgrains.

Within each subgrain there is a fine scale herring-bone shaped pattern indicated at H in Fig. 3c and schematically in Fig. 2b. The herring-bone pattern is shown at a larger magnification in Fig. 3d. It is composed of parallel bands with brighter or darker contrast. The thickness of the bands, nearly parallel to the $\{10\,\bar{1}\,1\}$ planes of the hexagonal structure, is in the range of 8–40 nm. The interfaces between the bands are not sharply defined. Within the bands there is a still finer structure which exhibits parallel bright and dark contrast stripes of ~ 2 nm width as indicated by short black bars at A in Fig. 3d. The herring-bone patterns and the finer stripes were caused by composition variations (see Section 3.4). The cross-section of the herring bone pattern in the plane normal to G (Fig. 3b) has a complex form, but the variation in composition is clear (see Section 3.4).

3.3. Electron diffraction

Electron diffraction data could provide useful information about the crystal structure and texture of the as-deposited Ti–Mg alloy.

A selected area electron diffraction pattern (Fig. 4a) was obtained from the middle of a columnar grain parallel to G shown in Fig. 3c. This pattern allows the following conclusions.

(1) The incident electron beam was along the $\langle 1\,\bar{2}\,1\,0\rangle$ direction of the h.c.p. lattice.
(2) A series of h.c.p. solid solutions are present with slightly different lattice parameters and they produce a radial extension of the diffraction maxima. Two of the diffraction peaks are dominant and their corresponding crystal directions and planes are nearly parallel to each other.
(3) The [0001] direction of the individual h.c.p. subgrains within each grain can vary by up to $\pm 5^\circ$ in orientation as is indicated by the angular extension of the diffraction peaks.

After the rotation correction between the images in Figs. 3c and 4a, the [0001] direction was determined to be along G, and the individual bands in the herring bone pattern in Fig. 3c as well as in Fig. 3d were nearly parallel to the $\{1\,0\,\bar{1}\,1\}$ planes. The diffraction patterns from adjacent grains were similar to that shown in Fig. 4a, which indicates that grains in the same columnar unit have an almost identical orientation.

The selected area diffraction pattern in Fig. 4b was taken from a grain belonging to another columnar unit about 30 μm away from the grain shown in Fig. 3c. The electron beam was parallel to $\langle 0\,\bar{1}\,1\,0\rangle$, and the [0001] direction was along G. It can be readily identified from Fig. 4b that the diffraction

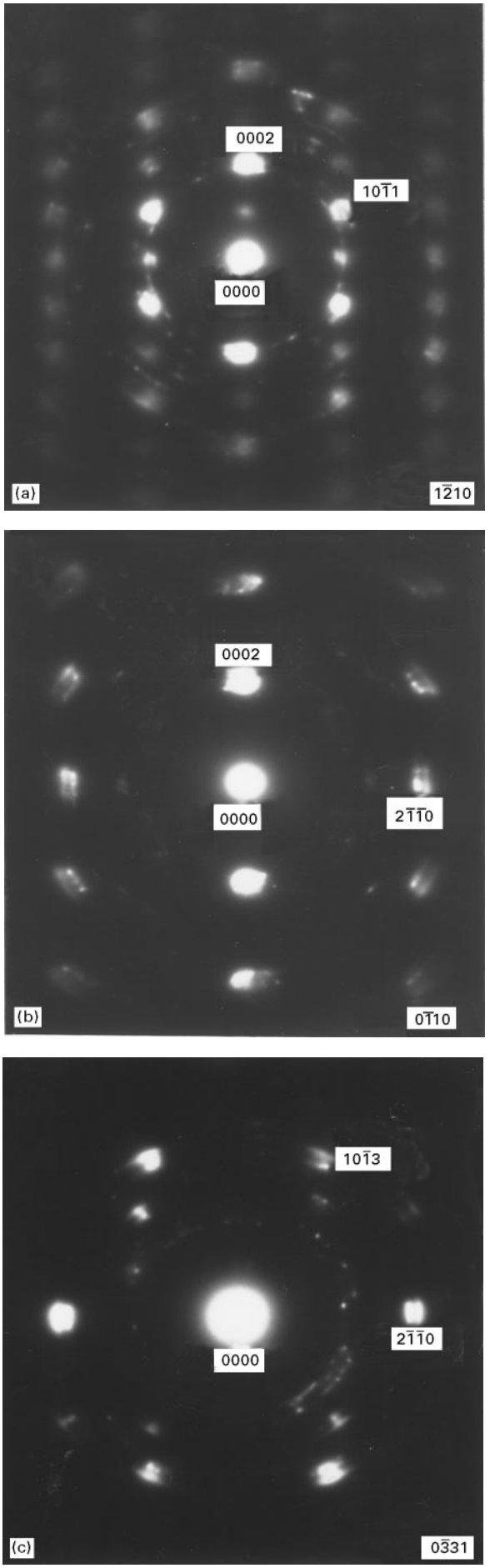

Figure 4 Selected area electron diffraction patterns from columnar grains in the foils parallel to G, showing the doubled spots and angular extension of the spots in the (a) $\langle 1\,2\,\bar{1}\,0\rangle$, (b) $\langle 0\,\bar{1}\,1\,0\rangle$ and (c) $\langle 0\,\bar{3}\,3\,1\rangle$ directions.

peaks are doubled and elongated, which again illustrates that there are two main h.c.p. solid solutions with different lattice constants and parallel corresponding lattice planes and directions, together with small orientational changes within the selected area. In order to obtain three dimensional orientational information, the sample was tilted from $\langle 0\,\bar{1}\,1\,0\rangle$ to $\langle 0\,\bar{3}\,3\,1\rangle$ through the $(2\,\bar{1}\,\bar{1}\,0)$ plane and a selected area diffraction pattern was taken (Fig. 4c). In this pattern, the diffraction peaks are still doubled and elongated, which leads us to the same conclusions as drawn from Fig. 4(a and b). Electron diffraction patterns from different columnar units (Fig. 4(a and b)) also indicate that there is a texture with [0001] nearly parallel to the deposit growth direction G in the alloy and a relative rotation around the [0001] direction among the units.

Although it was difficult to determine accurate values of the lattice parameters of the hexagonal phases from the electron diffraction patterns, the ratio of the lattice parameters could be obtained more accurately. The ratios of the lattice parameter $|a|$ are 1.08 and 1.06 as obtained from Fig. 4(a and b), respectively. These values are slightly smaller than 1.09, the ratio of the lattice parameter $|a|$ for pure metal Mg and Ti, which suggests that the two phases might be Ti–rich and Mg–rich Ti–Mg solid solutions, respectively. The ratio change from one region to another is possibly related to small changes of the composition in the different regions.

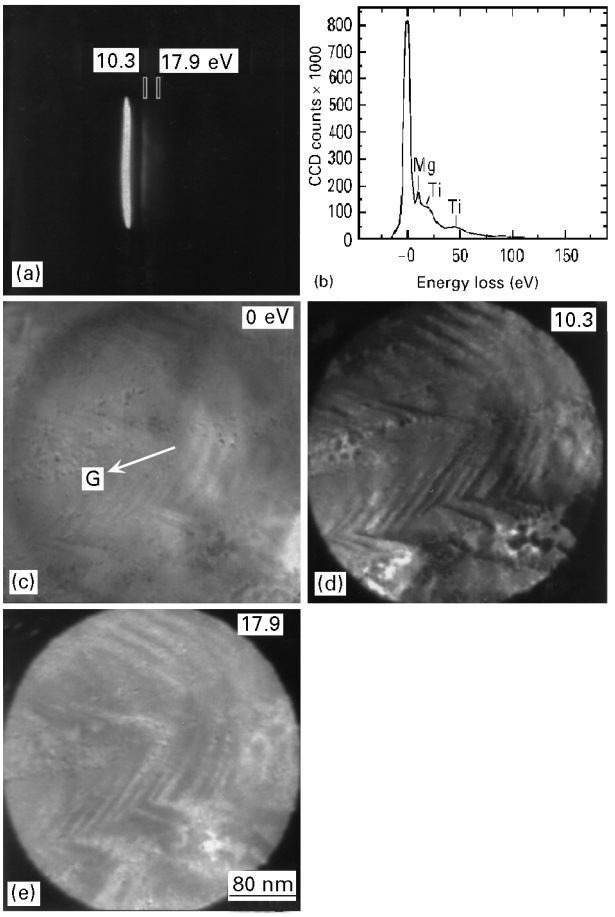

Figure 5 (a) PEELS spectrum and (b) its line profile of the Ti–29 wt % Mg alloy, showing electron energy-loss peaks at about 10.3, 17.9 and 48 eV, respectively. Imaging PEELS micrographs of a foil parallel to G, taken with electrons of energy-loss (c) 0 eV, (d) 10.3 eV (Mg) and (e) 17.9 eV (Ti), indicating that the herring-bone pattern is composed of alternating Mg-rich and Ti-rich bands.

3.4. Imaging PEELS

Imaging PEELS was performed in order to identify fine-scale composition changes in foils parallel and normal to the growth direction G.

A foil parallel to G was first selected. Fig. 5a shows a parallel electron energy loss spectrum and Fig. 5b its line profile. Two peaks at about 10.3 and 17.9 eV can be seen in Fig. 5a, which are more clearly shown on Fig. 5b. These peaks, which result from a mixture of collective excitations and interband transitions of the valence electrons, are related to Mg-rich and Ti-rich phases, respectively. Fig. 5b also shows a peak at 48 eV for the titanium M_{2-3} absorption edge. Fig. 5(c–e) are a set of micrographs taken from a columnar subgrain in a thin foil parallel to G using different energy–loss electrons. A 2 eV window was used in selecting the imaging electrons.

A zero-energy-loss micrograph shows weak contrast for the herring-bone pattern (Fig. 5c). The contrast was enhanced by moving the window to 10.3 eV (Fig. 5d) and reversed when the window was at 17.9 eV (Fig. 5e). The Mg-rich phase is located at the bright contrast bands in Fig. 5d, and the Ti-rich phase at the bright contrast bands in Fig. 5e which corresponds to the dark contrast bands in Fig. 5d. Fig. 5(c–e) indicates that the herring-bone pattern consists of bands of Ti-rich and Mg-rich phases which are arranged alternately, but at a slight angle to the growth direction G. The thickness of the bands is in the range of 8–40 nm. These observations are consistent with the microstructure shown in Fig. 3d and the compositional changes deduced from measurements on the electron diffraction patterns (Fig. 4(a and b)).

Another set of imaging PEELS micrographs (Fig. 6(a–d)) were taken at a higher magnification from a foil parallel to G and the peak at 48 eV for the titanium M_{2-3} absorption edge was used to map the distribution of titanium in bright contrast (Fig. 6d). The images at 0, 10.3 and 17.9 eV are shown in Fig. 6(a–c) respectively. The Mg plasmon-loss image (Fig. 6b) confirms that the dark contrast in Fig. 6d corresponds to a Mg-rich phase. Similar contrast was observed in Fig. 6(c and d) since the energy loss peaks at both 17.9 and 48 eV can be associated with a Ti-rich phase. Fig. 6(a–d) shows more clearly the alternating arrangement of Mg-rich and Ti-rich bands. It should be noted that the zero-energy-loss micrographs (Figs. 5c and 6a) also revealed a relationship between composition and contrast: Ti-rich bands were darker than Mg-rich bands because Ti atoms had a higher scattering power for electrons than Mg atoms.

Imaging PEELS sometimes revealed even finer structures within Mg-rich or Ti-rich bands. Fig. 7(a and b) are two micrographs of a foil parallel to G, imaged with Mg-related (10.3 eV) and Ti-related (17.9 eV) energy-loss electrons, respectively. Very fine parallel dark stripes, indicated by short bars on Fig. 7a, can be seen in a bright Mg-rich band.

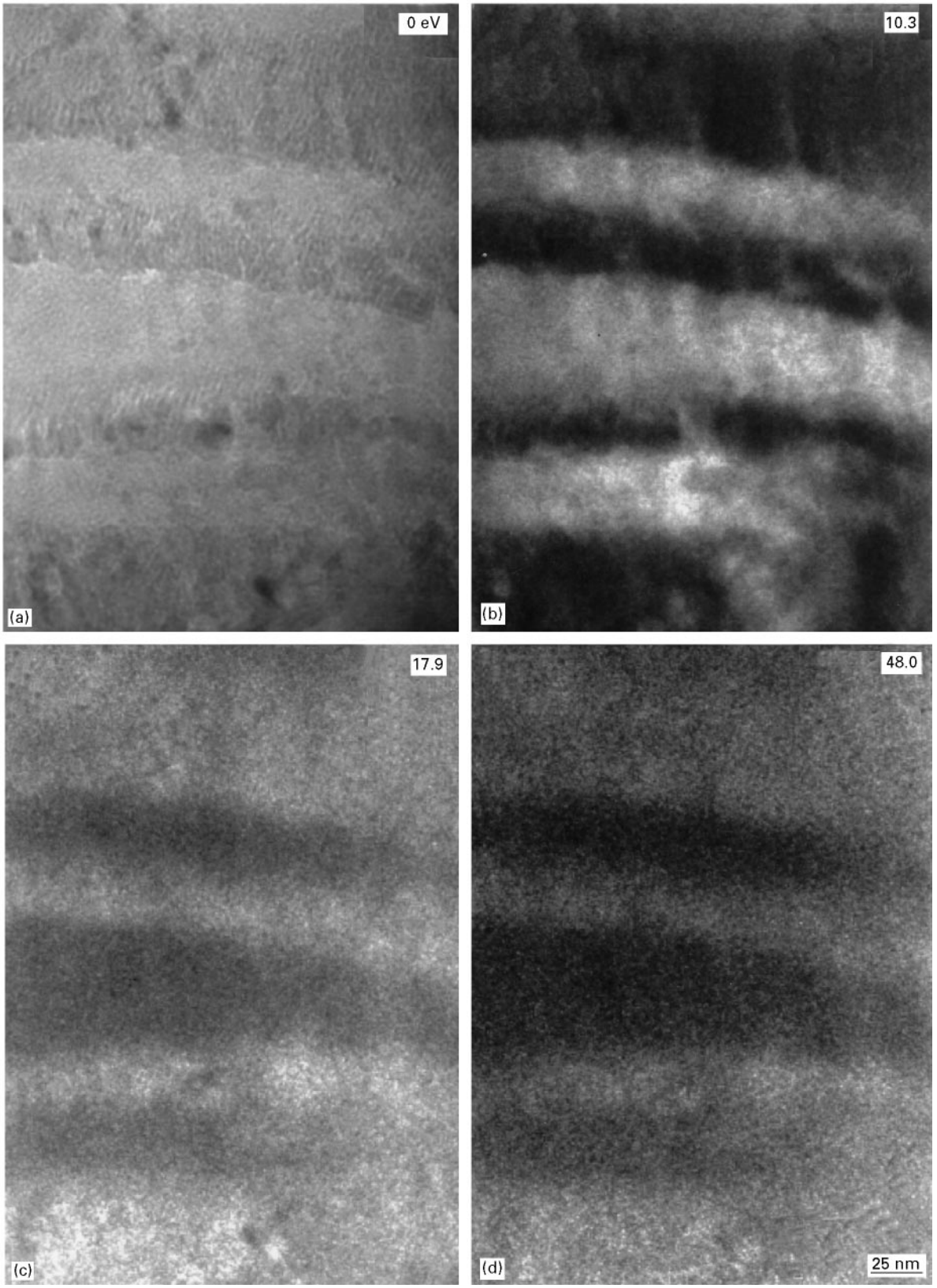

Figure 6 Imaging PEELS micrographs of a foil parallel to G, taken at higher magnification with electrons of energy-loss (a) 0 eV, (b) 10.3 eV (Mg) (c) 17.9 eV (Ti) and (d) 48.0 eV (Ti), showing alternating lamellae of Mg-rich and Ti-rich regions in different contrast.

These dark stripes in Fig. 7a become bright in Fig. 7b, and thus are related to Ti-rich regions. The thickness of these stripes is only about 2 nm, which is consistent with the features of the stripes at A in Fig. 3d.

A set of imaging PEELS micrographs (Fig. 8(a–d)) were also obtained from the same foil area as that shown in Fig. 3b to confirm the existence of the very fine scale Mg-rich and Ti-rich regions within subgrains. An image obtained with zero-energy-loss electrons (Fig. 8a) shows weak dark and bright contrast similar to that in Fig. 3b. The bright contrast of Fig. 8a was enhanced in Fig. 8b by selecting electrons at an energy loss of 10.3 eV, which corresponds to the

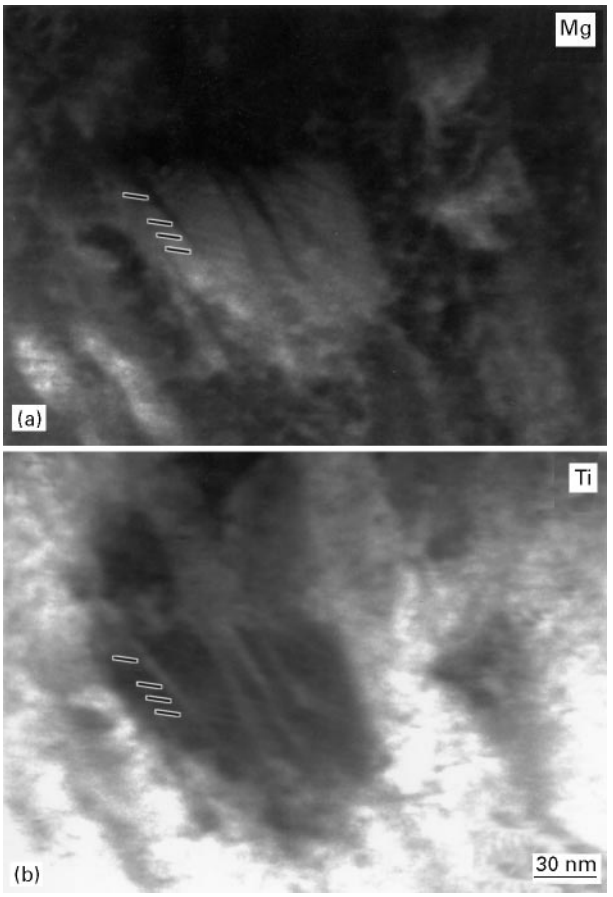

Figure 7 Imaging PEELS micrographs of a foil parallel to G, taken with electrons of energy-loss (a) 10.3 eV (Mg), (b) 17.9 eV (Ti), showing very fine structures in different contrast as indicated by short black bars within a Mg-rich band. The contrast change in the band is associated with compositional variations.

Mg-rich regions. The dark contrast of Fig. 8a remained in Fig. 8b, but changed to a bright contrast in Fig. 8(c and d), and therefore indicated the size, shape and distribution of the Ti-rich regions in the section perpendicular to G.

3.5. Twin boundaries

In addition to the band-like Mg-rich and Ti-rich regions evident in thin foils parallel to G, there are also twin boundaries parallel to the $\{1\,0\,\bar{1}\,1\}$ planes within the Mg-rich or Ti-rich bands, or alternating twin-like relationships between the Mg-rich and Ti-rich bands.

Fig. 9a shows a selected area electron diffraction pattern taken from a columnar subgrain in a foil parallel to G with the electron beam parallel to the $\langle 1\,\bar{2}\,1\,0\rangle$ direction of the hexagonal phase. It should be noted that each peak in Fig. 9a is actually doubled due to contributions from both Mg-rich and Ti-rich regions: there are in fact four sets of superimposed electron diffraction patterns, any two of which either share their $\{1\,0\,\bar{1}\,1\}$ peaks or else have parallel $\{1\,0\,\bar{1}\,1\}$ planes. Fig. 9b shows a schematic diagram of the four sets of electron diffraction patterns marked by T1, T2, M1 and M2, respectively. T1 and T2 arise from the Ti-rich solid solution, and M1 and M2 from the Mg-rich solid solution. Fig. 9(c and d) are two dark field micrographs taken using the (0001) peaks corresponding to the T1M1 and the T2M2 sets in Fig. 9b. The boundary marked between the dark and bright regions is parallel to the $\{1\,0\,\bar{1}\,1\}$ plane. There are four possible orientation relationships between the adjacent regions on either side of the boundaries, as is shown in Fig. 9(e–h). Fig. 9(e and f) show mirror twin-relationships between the two regions of the same composition. In Fig. 9(g and h), we show the boundary connects regions of different compositions. In these cases the boundary is not a true twin boundary because the diffraction peaks of the regions cannot be superimposed by a mirror operation, although their corresponding directions could. We shall call such a boundary "twin-like".

3.6. Periodic compositional variation

In addition to the fine-scale compositional variations associated with the herring-bone patterns within the subgrains, a further periodic compositional change was also observed. It differs from the herring-bone structure in that the composition variation is in planes parallel to the growth surface, and the scale of the periodic compositional change is greater.

The additional compositional variation is revealed in Fig. 3c by the weak horizontal bands normal to G. Fig. 10a is a bright-field micrograph taken from a thicker region of a thin foil parallel to G, and clearly shows alternate bright and dark contrast bands. These bands are perpendicular to G with a periodicity of about 0.5 μm. Fig. 10b shows the integrated intensities for the Mg K_α and Ti K_α peaks on the EDX traces obtained from several consecutive dark and bright bands observed in Fig. 10a. For the Mg peak intensities, the value at B corresponding to a bright band is a little higher than those at adjacent dark bands D. For Ti peak intensities, the result is reversed, that is, the value at B is lower than that at adjacent dark fringes. Fig. 10c shows the ratios of the integrated intensities related to the Ti K_α and Mg K_α peaks, respectively, at the position of the bands. The values of the ratios at the bright bands are lower than those at the dark bands. It is well-known that under the experimental conditions used the ratio of integrated intensities can be directly related to the element content. Although Fig. 10(b and c) are uncalibrated at present and therefore do not give quantitative information on the composition, they clearly exhibit a compositional variation along G. The Ti content at the position of the bright bands in Fig. 10a is lower than that at the position of the dark bands as anticipated.

4. Discussion

The vapour-quenched Ti–29 wt % Mg alloy collected at 300 °C has a complex microstructure. It contains orientation-textured columnar units, columnar grains, columnar subgrains, a herring-bone pattern and parallel stripes on scales ranging from 15 μm to 2 nm and is superimposed by periodic compositional variations of a ~ 0.5 μm wavelength along the deposit growth

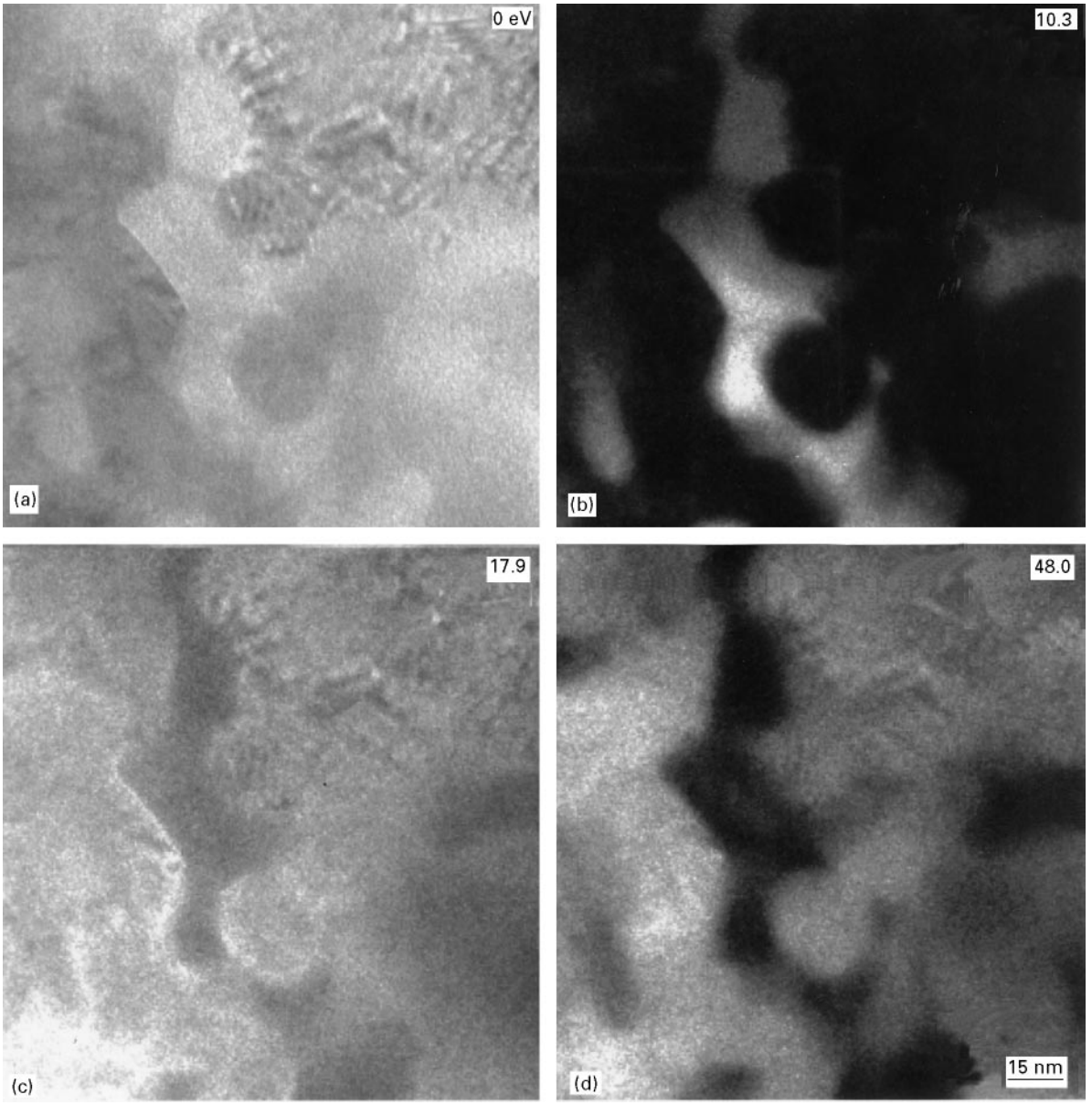

Figure 8 Imaging PEELS micrographs from an area shown in Fig. 3b, taken with electrons of energy-loss (a) 0 eV, (b) 10.3 eV (Mg), (c) 17.9 eV (Ti) and (d) 48.0 eV (Ti), showing Mg-rich and Ti-rich regions in different contrast.

direction. The results confirm that the Ti–29 wt % Mg alloy is composed of Ti–Mg solid solutions with local variations in solute concentration in Ti-rich and Mg-rich regions. The highly alloyed Ti–Mg alloy microstructure differs from a dilute alloy microstructure by having herring-bone patterns and parallel stripes which can be associated with composition variations on a nanometre scale. It is therefore not surprising that the alloy proved difficult to analyse using conventional X-ray techniques.

The present studies can help to explain the broad peaks observed on the X-ray diffraction patterns reported previously [13]. The X-ray diffraction patterns are average results obtained from probed regions of a size of several μm. Since the density of dislocations in the alloy is not particularly high, the strain and composition variations in the probed regions are probably the main factors that are responsible for the broad peaks observed on the X-ray diffraction patterns.

The strain might be caused by lattice parameters differences between the Ti-rich and Mg-rich solid solutions. From Fig. 3(a and b), the strain between the two solid solutions was calculated to be in the range of 6–8%. The small dimension of the Ti and Mg rich regions should lead to a higher ratio between the strained and unstrained regions. The strain might also result from the misorientation of the regions either with similar or with different compositions and from cooling stresses.

The compositional variation with the period of 0.5 μm (Fig. 10a) could make a significant contribution since the X-ray probed area covers several periods of the compositional variation. The lattice parameters of the Ti–Mg solid-solution alloy are directly related to its composition [13]. The compositional variation in the probed area produces the simultaneous appearance of diffraction peaks at slightly different positions. If the individual peaks are indistinguishable then they will form a single broad

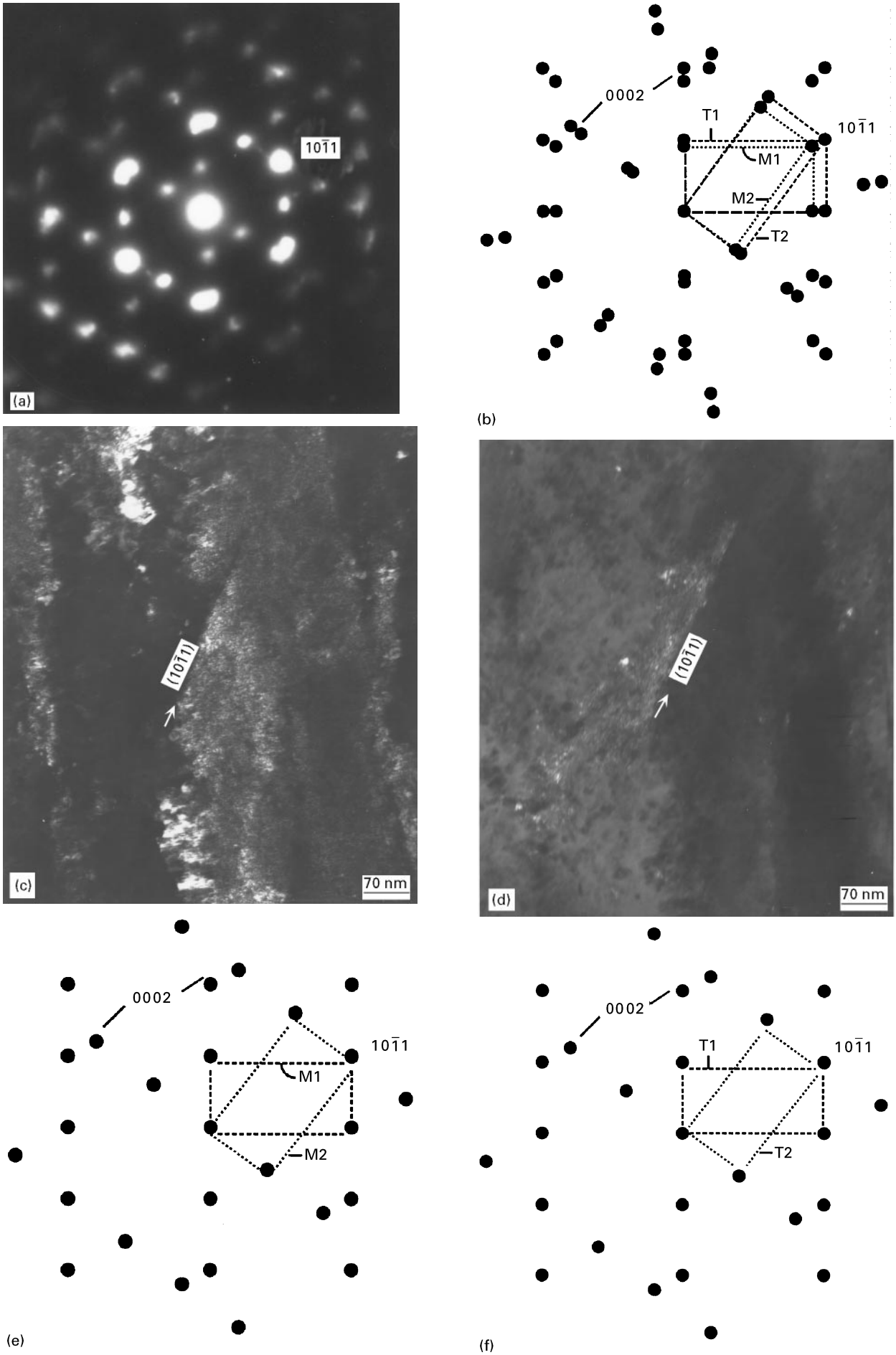

Figure 9 (a) Selected area electron diffraction pattern taken in the $\langle 1\,2\,\bar{1}\,0\rangle$ direction. (b) Schematic diagram of (a), illustrating there are four sets of patterns marked by T1, T2, M1 and M2, and their relationship. (c) and (d) Dark field micrographs taken using the 0001 spots belonging to T1M1 and T2M2 sets, respectively, showing a boundary parallel to the $\{1\,0\,\bar{1}\,1\}$ plane. (e), (f), (g) and (h) display four possible relationships between two sides of the boundary.

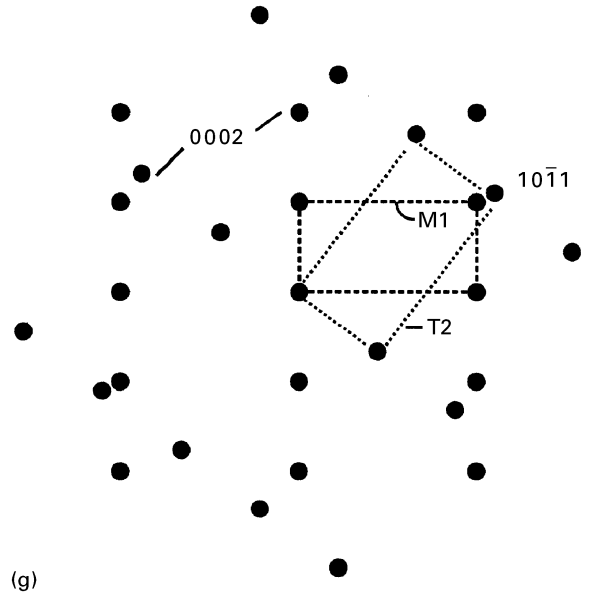

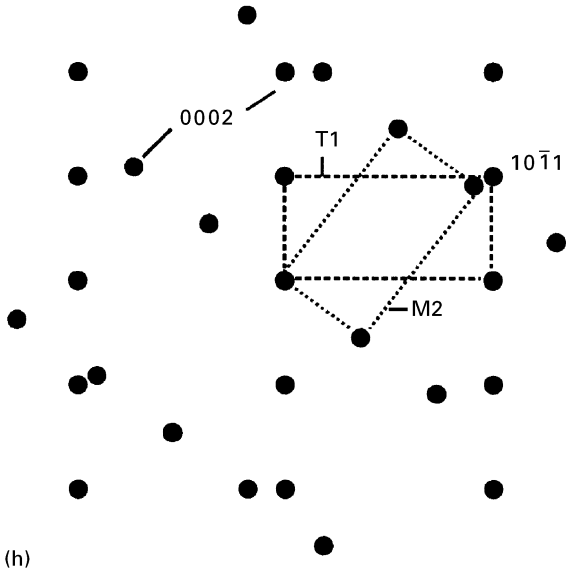

Figure 9 continued.

peak. The presence of twin or twin-like boundaries could further broaden the X-ray diffraction peaks, however they should not be the main broadening factor in this alloy because of their relatively low density.

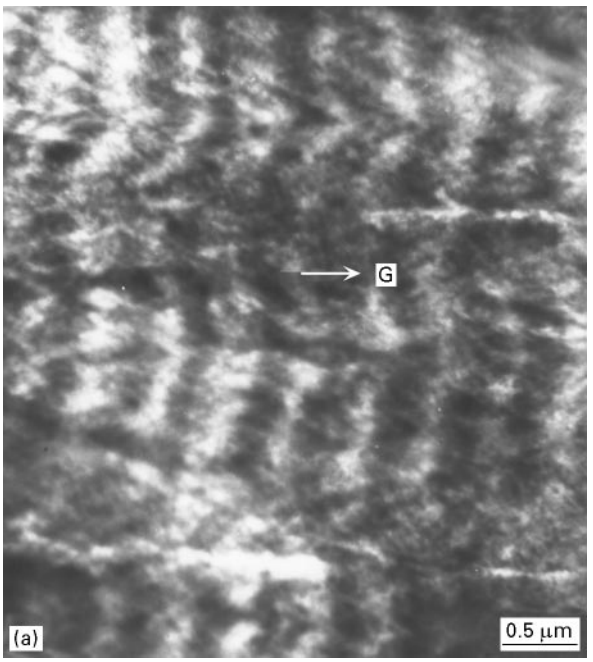

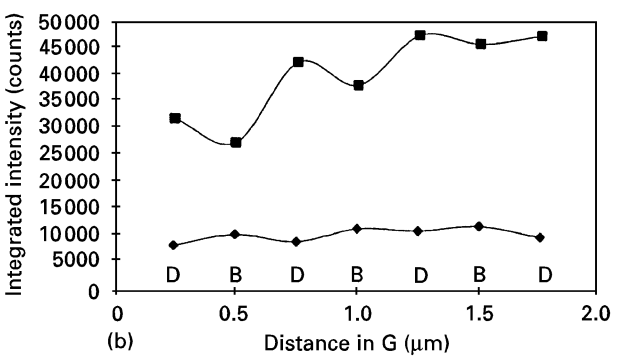

The various compositional changes observed within the alloy can be attributed to several different factors. The 0.5 μm periodicity might be related to periodic changes at the evaporating surface of the Ti target as a result of instability of the bombarding electron beam. The temperature instability of the radiantly heated Mg source could cause a much coarser composition change, which should be avoided. The formation of the lamellar Ti-rich and Mg-rich h.c.p. regions might be the result of local movement of the Ti and Mg atoms just beneath the growth surface during the crystal growth. The present Ti–Mg alloy was deposited on to a pure Ti substrate maintained at 300 °C. The average growth rate was $\sim 14\,\mu m\,s^{-1}$ and the deposition process lasted 130 min. Atomic movement during the alloy growth could have occurred during (a) the quenching of the deposit to 300 °C and (b) ageing it at 300 °C. Based on the reported effects of annealing temperature and time [13], the first case probably has the greatest effect on the atomic movement, but it is restricted to regions just beneath the growth surface. This might explain why the orientation of the Ti-rich and Mg-rich lamellae was observed to be approximately parallel to the tapered (1 0 $\bar{1}$ 1) growth surfaces.

Figure 10 (a) Bright field TEM micrograph showing periodic bands with a period of about 0.5 μm. (b) Integrated intensities under (◆) Mg K_α and (■) Ti K_α peaks on EDX spectra obtained from consecutive dark and bright bands in (a). (c) The ratio of the integrated intensities in (b).

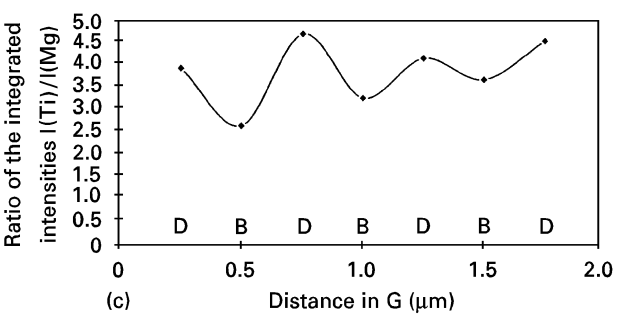

Acknowledgements

Authors would like to thank R. Vincent, P. Midgley and K. E. Bagnall for their help. Financial support from the DRA is gratefully acknowledged by the authors from the University of Bristol.

References

1. C. M. WARD-CLOSE and P. G. PARTRIDGE, *Mater. Lett.* **11** (1991) 295.
2. E. W. GOLIBER and K. H. McKEE, in "Progress in very high pressure research", edited by F. P. Bundy, W. R. Hibbard, Jr., and H. M. Strong (John Wiley, New York, 1961) p. 126.
3. R. A. ORIANI and H. M. STRONG, *Trans. AIME* **236** (1966) 1508.
4. L. C. FINCHER and D. H. DESY, *ibid.* **242** (1968) 2069.
5. V. I. DOBOTKIN, N. F. ANOSHKIN and A. G. PAVLOV, in "Titanium 80 Science and technology", Vol. 3, edited by H. Kimura and O. Izumi (TMS-AIME, Warrendale, PA, 1980) p. 2153.
6. J. W. FREDERICKSON, *Trans. AIME* **203** (1955) 368.
7. P. S. GILMAN and J. S. BENJAMIN, *Ann. Rev. Mater. Sci.* **13** (1983) 279.
8. F. H. FROES, *Mater. Sci. Engng.* **A117** (1989) 19.
9. J. L. MURRAY, "Phase diagrams of binary titanium alloys", (ASM International, Metals Park, OH, 1987).
10. D. M. J. WILKES, P. S. GOODWIN, C. M. WARD-CLOSE, K. BAGNALL and J. W. STEEDS, *Mater. Lett.* **27** (1996) 47.
11. *Idem*, in "Metastable phase and microstructures", Mat. Res. Soc. Symp. Proc. Vol. 400, edited by R. Bormann, G. Mazzoni, R. D. Shull, R. S. Averbach, R. F. Ziolo (MRS, Pittsburg, P. A., 1996) p. 267.
12. C. M. WARD-CLOSE, D. M. J. WILKES, P. S. GOODWIN, P. G. PARTRIDGE and K. BAGNALL, in Proceedings of the 8th World Conference on Titanium, Burmingham, 22–26 October edited by P. A. Blenkinsop, W. J. Evans and H. M. Plower (Institute of Materials, 1996) p. 2673.
13. C. M. WARD-CLOSE, P. G. PARTRIDGE, P. HOLDWAY and A. W. BOWEN, in "Titanium 92 science and technology", edited by F. H. Froes and I. R. Caplan (TMS, Warrendale, PA, 1993) p. 659.
14. C. M. WARD-CLOSE, P.G. PARTRIDGE and C. J. GILMORE, *ibid*., p. 651.
15. C. M. WARD-CLOSE, G. LU and P. G. PARTRIDGE, *Mater. Sci. Engng.* **A189** (1994) 247.
16. G. LU, P. G. PARTRIDGE, C. M. WARD-CLOSE and J. W. STEEDS, *J. Mater. Sci.* **31** (1996) 867.

Received 20 November
and accepted 19 December 1996